Journal of
Materials Chemistry A

Accepted Manuscript

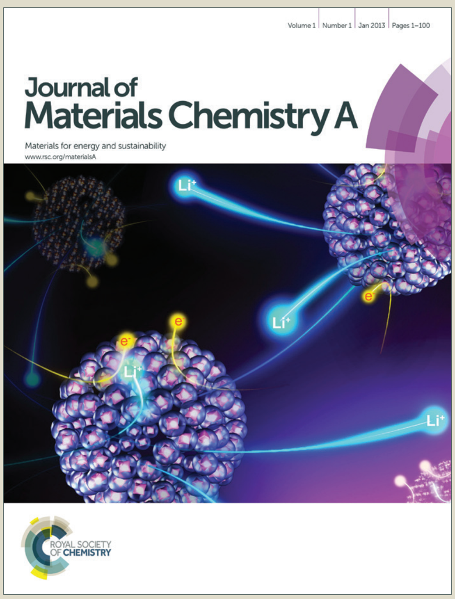

Better Lithium-Ion Storage Materials Made through Hierarchical Assemblies of Active Nanorods and Nanocrystals

Chao Lei,[a,b] Zheng Chen,[b] Hiesang Sohn,[b] Xiaolei Wang,[b] Zaiyuan Le,[b] Ding Weng,[b] Meiqing Shen,[a] Ge Wang[c]* and Yunfeng Lu[b]*

[a]*Key Laboratory for Green Chemical Technology of the Ministry of Education, School of Chemical Engineering and Technology, Tianjin University, Tianjin, 30072, P. R. China,*

[b]*Department of Chemical and Biomolecular Engineering, University of California, Los Angeles, CA 90095, USA, E-mail: luucla@ucla.edu*

[c]*School of Materials Science and Engineering, University of Science and Technology Beijing, Beijing, 100083, China, E-mail: gewang@mater.ustb.edu.cn*

Abstract

Lithium-ion storage materials with significantly improved performance were developed through hierarchical assemblies of vanadium-based oxide (V_2O_5 and LiV_3O_8) nanorods or iron oxide (Fe_3O_4) nanocrystals using an efficient, continuous aerosol-spray process. Such hierarchically porous spheres, which were made from networks of low-dimension building blocks, offer the materials with shorten ion-diffusion length, fast electrolyte diffusion, and structural robustness. Resulted from their unique hierarchical structure, these spheres exhibit high lithium storage capacity, excellent cycling stability and good rate capability. This work offers a novel synthesis approach towards better lithium-ion storage materials.

Keywords

hierarchical assembly, lithium-ion storage, aerosol-spray, vanadium oxide, iron oxide

Introduction

Lithium-ion batteries (LIBs) are important energy storage devices for broad uses in portable electronics, hybrid electric vehicles and many other devices [1]. Current lithium-ion electrodes are often made from micron-size particles of active materials, which may result in low rate-capability due to inefficient charge transport. To address this problem, active materials with low-dimension forms (e.g., nanoparticles, nanowires and nanorods) have been extensively explored [2-5]. While the use of low-dimension materials shortens the ion transport length, it also creates more interfaces between the active materials and the other electrode components (e.g., electrolyte, binder, and conductive agent), which may cause performance deterioration during electrode charge/discharge cycling. Materials with hierarchical structures have shown great interest since they can provide both low-dimensional charge transport properties and better interfacial stability than their nanoscale building blocks. So far great effect has been devoted to design and synthesis of hierarchical electrode materials, such as V_2O_5[6], TiO_2[7], SnO_2[8], Si/Carbon[9] $Li_4Ti_5O_{12}$[10] and $LiFePO_4$[11]. However, making these materials is often based on batch-by-batch hydrothermal reaction with special structure directing agents or multi-step deposition/coating techniques, thus limiting the large scale application of such materials.

To address this challenge, we present herein a general structure design of electrode material based on a simple and continuous aerosol-spray synthesis, where nanorods or nanocrystals of the electrode active materials were assembled into robust network spheres. To demonstrate this concept, vanadium oxide (V_2O_5 and LiV_3O_8) and iron oxide (Fe_3O_4) were used respectively as the model cathode and anode materials. Both vanadium oxide and iron oxide are promising candidates for LIBs due to their high capacity, low cost and abundance. Although the average voltage of V_2O_5 and LiV_3O_8 is a little lower than that of $LiCoO_2$ and $LiMn_2O_4$, the capacity of V_2O_5 and LiV_3O_8 is about twice of these commercial cathode materials. For example, based on the intercalation of 2.5 lithium-ion (1.8-4.0 V) and 4 lithium-ion (2.0-4.0 V), a theoretical capacity of ~350 and ~372 mAh g^{-1} may be achieved for V_2O_5 and LiV_3O_8, respectively [6,12-15]. Similarly, Fe_3O_4 holds a theoretical capacity of ~926 mAh g^{-1}, which is significantly larger than that of the commercial graphite anode [16,17]. However, both vanadium oxide and iron oxide show low lithium-diffusion coefficient, poor electronic conductivity and structure instability during cycling [18-20]. Although various low-dimension vanadium oxide and iron oxide based structures (e.g., nanorods [21-23], nanowires [24-26], and nanoparticles [27-29]) have been developed with enhanced lithium intercalation kinetics, as explained above, such materials show rapid capacity decay due to structure failure.

Through a simple but efficient aerosol-spray synthesis, micron-size particles can be effectively formed in such a continuous process. These particles will be constructed by vanadium oxide nanorods or Fe_3O_4 nanocrystals, which are connected into robust porous networks through strong covalent, metallic or ionic bonds. Such micron-size particles, mesoscopically, still retain the low-dimension structure with shortened transport length ensuring better rate performance. Moreover, as-formed network structure provides the particles with mechanical robustness, which enables them to resist mechanical and chemical stress that may be generated during the charge/discharge process. Due to the unique structure, such a simple strategy provides the materials with significantly improved performance for lithium storage, shining light for their large-scale application. Note that aerosol- and ultrasonic-spray method has been used to make electrode materials (e.g., Sn/C[30], $LiNi_{1/3}Co_{1/3}Mn_{1/3}O_2$[31], but few of them showed hierarchical structure (Si/C composite[32]). Our work provides a general approach that can use various precursors (either salt or colloidal particle solution) to make hierarchical structured electrode materials.

1. Experimental

1.1 Synthesis of V_2O_5 and LiV_3O_8 nanorod spheres

In a typical synthesis, 0.4 g of commercial V_2O_5 (98%, Aldrich) and 3.2 mL of nitric acid (HNO_3) (70%, Sigma-Aldrich) were dissolved in 40 mL of de-ionized water, forming a homogenous light-yellow precursor solution. Then, 0.4 g of block copolymer F127 ($EO_{106}PO_{70}EO_{106}$, M_w = 12600 g mol^{-1}, where EO and PO represent ethylene oxide and propylene oxide, respectively) was added into the solutions after stirring for 6 h. The solutions were stirred vigorously for another 12 h before the aerosol-spray process. A homemade aerosol generator was employed to synthesize the nanorod spheres. During the aerosol-spray process, the solutions were delivered via the nitrogen carrier gas to the atomizer nozzle to generate micro-droplets. Then the aerosol droplets were passed through the heating zone set at 400 °C. The resultant powder product was collected on a 450 nm filter paper. The as-synthesized particles were then sintered at 400 °C in air for 6 h to obtain nanorod spheres.

The synthesis of LiV_3O_8 nanorod spheres was conducted using a similar process. In a typical preparation, 0.4 g of commercial V_2O_5 (98%, Aldrich) and 3.2 mL of HNO_3 (70%, Sigma-Aldrich) were dissolved in 40 mL of de-ionized water, forming a homogenous light-yellow precursor solution. Next, 0.054 g of Li_2CO_3 (99%, Sigma-Aldrich) was added, and the mixture was actively stirred for 6 h. Then, 0.42 g of F127 was added into the solutions. The solutions were stirred vigorously for 12 h before the aerosol-spray process.

1.2 Synthesis of Fe_3O_4 nanocrystal spheres

To make nanospheres, the Fe_3O_4 nanocrystals were first synthesized through a co-precipitation method reported by Chen *et al.*[33] Typically, 1.113 g of $FeCl_2 \cdot 4H_2O$ (99%, Aldrich) and 3.027 g of $FeCl_3 \cdot 6H_2O$ (97%, Sigma-Aldrich) were dissolved in 150 mL of de-ionized water in a 250 mL three-neck flask. The mixture solution was heated to 50 °C and vigorously stirred under a nitrogen atmosphere. Then, 12.5 mL of aqueous ammonia solution (28%, Sigma-Aldrich) was rapidly poured into the solution with an immediate color change to black. After that, the reaction solution was cooled down to room temperature after reaction for 30 min. The Fe_3O_4 nanocrystals were collected by rinsing with de-ionized water for three times.

0.4 g of as-prepared Fe_3O_4 nanocrystals was dissolved in 40 mL of de-ionized water, sonicating for 2 h to form a homogenous precursor solution. A homemade aerosol generator was employed to synthesize the nanocrystal spheres. During the aerosol-spray process, the solutions were delivered via nitrogen carrier gas (40 psi) to the atomizer nozzle (TSI model 3076) to generate micro-droplets. Then the aerosol droplets were passed through the heating zone in a tube furnace set at 450 °C. The resultant powder product was collected at the end of the furnace and then sintered at 400 °C under an argon atmosphere for 4 h to obtain nanocrystal spheres.

1.3 Structural Characterization and Electrochemical Measurements

The x-ray diffraction (XRD) patterns were obtained with an X'Pert Pro X-ray powder diffractometer operating at 45 kV and 40 mA equipped with nickel-filtered Cu Kα radiation (λ = 1.5418 Å). The grain sizes of V_2O_5 sphere were calculated by JADE 5, determined by peaks of (110) reflection, using the Scherrer equation, $d = (0.9 \cdot \lambda/\beta \cos \theta)$, where the λ is the wavelength of the x-ray, β is the full width at half maximum (FWHM) corrected for instrumental broadening, and θ is the Bragg angle of the diffraction peak. Nitrogen adsorption/desorption isotherms were obtained using a Micromeritics ASAP 2020 analyzer.

The specific surface areas were calculated using N_2 adsorption branch at 77 K by the Brunauer–Emmett–Teller (BET) method. Pore size distributions (D_p) were derived from the adsorption branches of isotherms. Prior to the measurement, all samples were degassed at 200 °C under vacuum for 4 h. The relative pressure of BET calculation is P/P_0= 0.05～0.25. SEM and TEM were conducted on a JEOL JSM-6700 FE-SEM and Philips CM120 instrument, respectively.

The electrodes were fabricated by coating slurries containing 80 wt-% of active material, 10 wt-% of carbon black and 10 wt-% of PVDF binder dispersed in NMP (N-methylpyrrolidinone) on stainless substrates, and dried at 90 °C for 12 h under vacuum. Cell assembly was carried out in an argon-filled glovebox with moisture and oxygen below 1 ppm. 1.0 M $LiPF_6$ in ethylene carbonate (EC)/dimethyl carbonate (DMC) (1:1 in volume ratio) was used as the electrolyte. For the V_2O_5 nanorod spheres, the typical electrode loading was about 2.7 mg cm^{-2} (active material). The charge/discharge tests were performed over the potential region of 1.8~4.0 V with different rates on LAND CT2000 battery tester. Cyclic voltammetry (1.8~4.0 V, 1 mV s^{-1}) was conducted in a Bio-Logic VMP3 electrochemistry workstation. For the LiV_3O_8 nanorod spheres, the typical electrode loading was about 3.0 mg cm^{-2}. The charge/discharge tests were performed over the potential region of 2.0~4.0 V with different current densities. For the Fe_3O_4 nanocrystal spheres, the typical loading was about 2.9 mg cm^{-2}. The charge/discharge tests were performed over the potential region of 0.005~3.0 V with a current density of 100 mA g^{-1}.

2. Results and Discussion

2.1 V_2O_5 nanorod spheres

Figure 1 illustrates our synthesis strategy based on a simple aerosol-spraying process. For example, we started with homogenous solutions prepared by dissolving commercial V_2O_5 powder in acidic surfactant solution. Atomization process using nitrogen as the carrier gas continuously generated aerosol droplets, which were passed through a heating zone and converted to homogenous V_2O_5 nanocomposite particles. Subsequent sintering process removed the surfactant, induced growth of V_2O_5 nanorods within the particles and resulted in the formation of porous spheres hierarchically constructed from networks of the nanorods.

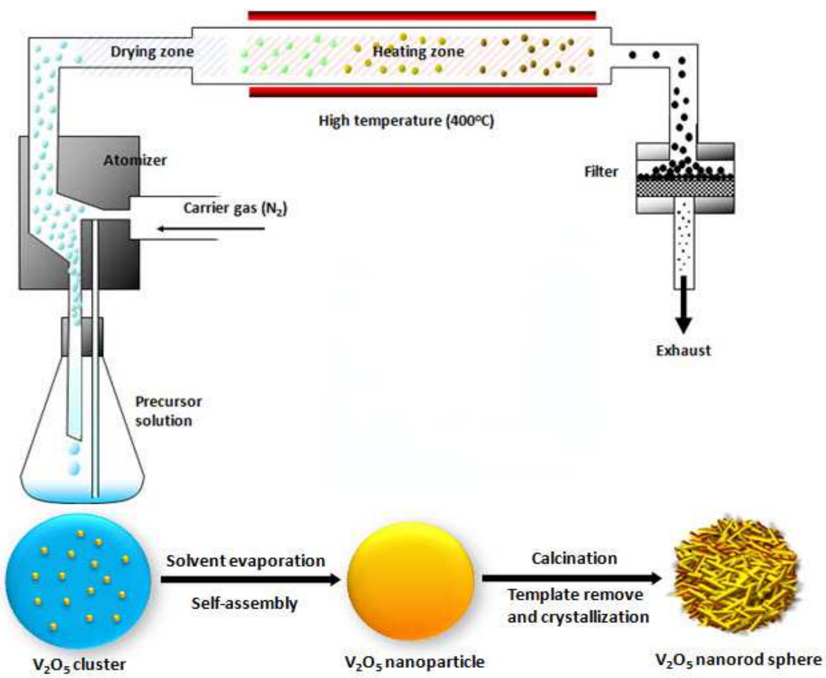

Figure 1. Schematic illustration of the synthesis of V_2O_5 nanorod-spheres by aerosol spraying.

Figure 2a shows a scanning electron microscopy (SEM) image of the V_2O_5 particles with diameters ranging from 100 to 500 nm. Each particle is made from nanorods with diameters of about 20-40 nm and length of about 100 nm (inset of Figure 2a). Figure 2b shows transmission electron microscopy (TEM) images of the V_2O_5 particles, clearly confirming that these nanorods are interweaved into porous networks. The inset of Figure 2b further confirms the small dimension of the nanorods with abundant mesopores with pore size of 20-30 nm. Figure S1 shows nitrogen adsorption/desorption isotherms and pore size distribution of V_2O_5 nanorod spheres and commercial V_2O_5 particles, both of which are similar in shape. Compared with commercial V_2O_5 particles, the V_2O_5 nanorod spheres exhibit higher surface area and larger pore volume, which is consistent with the SEM and TEM observations (Table S1). Although their average pore sizes are similar, the V_2O_5 nanorod spheres possess abundant mesopores, leading to the formation of a hierarchically porous structure that facilitates the transport of lithium ions.

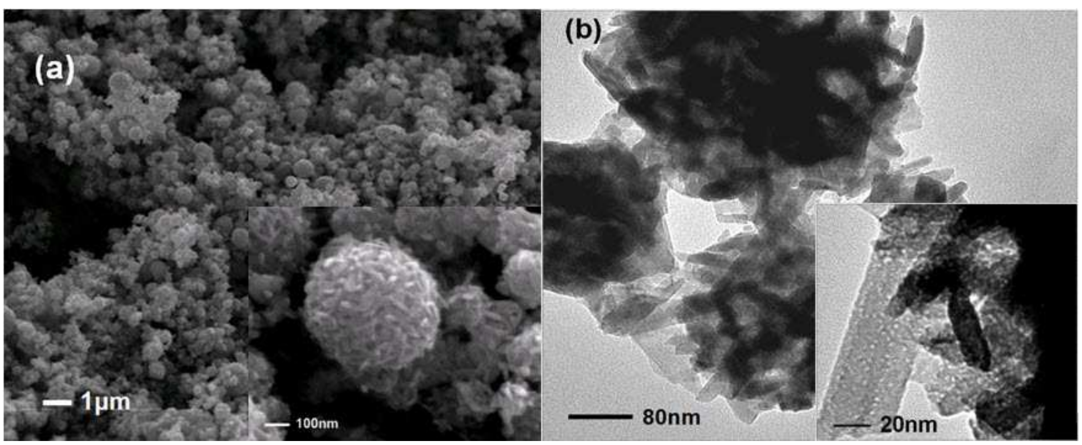

Figure 2. (a) SEM and (b) TEM images of the nanorod spheres.

To understand the growth mechanism of the V_2O_5 nanorod spheres, we further investigated the morphological and structural evolution of the particles using electron microscopic and x-ray diffraction (XRD) techniques (Figure 3 and Figure 4). It was found that the as-synthesized particles (prior to the sintering process) show non-porous, smooth and uniform spherical structure (see the SEM image in Figure 3a and TEM image in Figure 3e);

XRD suggests an amorphous nature of such particles (Figure 4a). After sintering at 250 °C for 1 h, the surfaces of the particles became rough (Figure 3b, f) and the crystalline phase appeared (Figure 4a). The crystalline structure further developed with increasing temperature to 300 °C and 400 °C (Figure 4a); consistently, nanorods of the V_2O_5 were developed gradually leading to the formation of nanorod spheres at 400 °C.

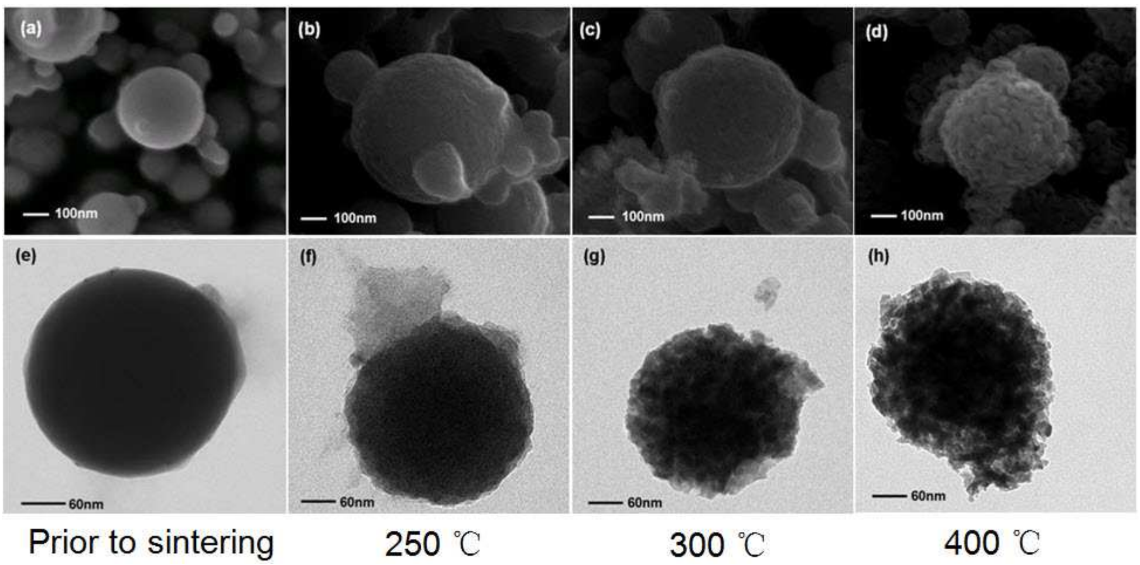

Figure 3. SEM (a-d) and TEM (e-h) images of the V_2O_5 particles prior to and after sintering at 250 °C, 300 °C, and 400 °C for 1 h in air.

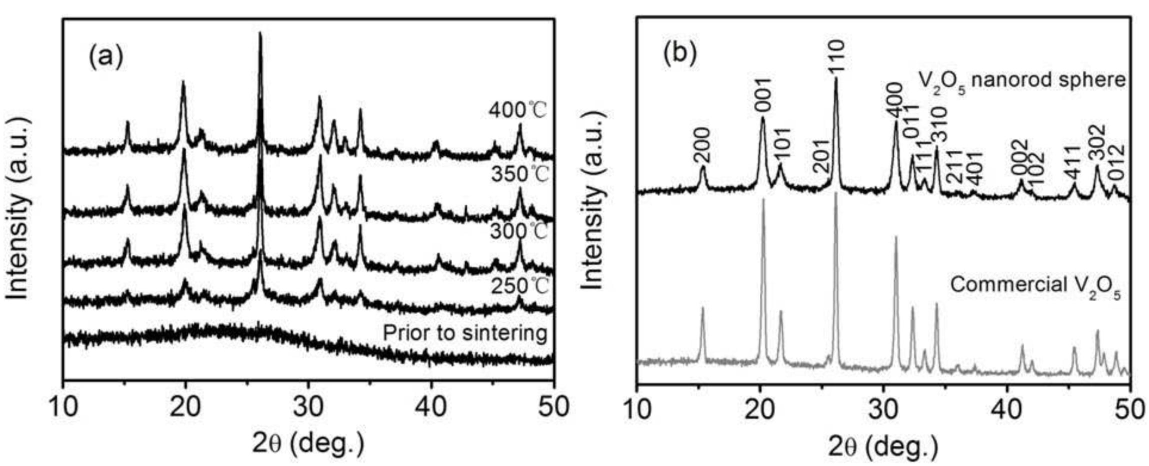

Figure 4. (a) XRD patterns of the V_2O_5 nanorod spheres sintered at different temperatures indicating their crystalline structure evolution and (b) XRD patterns of the V_2O_5 nanorod spheres and the commercial V_2O_5 particles.

The crystalline structure of the V_2O_5 nanorod spheres after sintering at 400 °C were further compared with that of the commercial one (Figure 4b). All the diffraction peaks of the nanorod spheres agree well with those of the commercial V_2O_5, which can be assigned to an orthorhombic phase with a space group of *Pmmn* (a = 11.516 Å, b = 3.5656 Å, c = 4.3727 Å). The diffraction peaks of the nanorod spheres show lower intensity and broader width, suggesting smaller crystallites. According to the Scherrer equation, the average grain size of the nanorod spheres is around 32.8 nm estimated from the (110) reflection, which is smaller than that of the commercial one (50.4 nm).

The lithium storage behavior of the V_2O_5 nanorod spheres was first characterized by cyclic voltammetry (CV) test in three-electrode cells using lithium foils as both the reference and counter electrodes. As shown in Figure 5a, in agreement with previous studies, two pairs of redox peaks can be observed in the high voltage window of 2.8–4.0 V, usually corresponding to lithium-ion intercalation into α-V_2O_5 to form ε-$Li_{0.5}V_2O_5$ and δ-LiV_2O_5, respectively. In the low voltage window of 1.8–2.8 V, another pair of redox peaks can be also noted, which is attributed to more lithium-ion intercalation into δ-LiV_2O_5 to form γ-$Li_2V_2O_5$ and ω-$Li_3V_2O_5$, respectively [34,35]. In comparison, a commercial V_2O_5-based electrode was also fabricated and tested at the same condition. It can be observed that the nanorod-spheres-based electrode has a larger CV area than that of the commercial V_2O_5-based electrode, indicating a higher charge-storage capacity. In addition, the commercial V_2O_5 electrode presents similar intercalation/de-intercalation peaks, though the peak separation of the commercial-V_2O_5 electrode is significantly larger than that of the nanorod-sphere electrode, indicating a larger polarization due to inefficient ion transport [36].

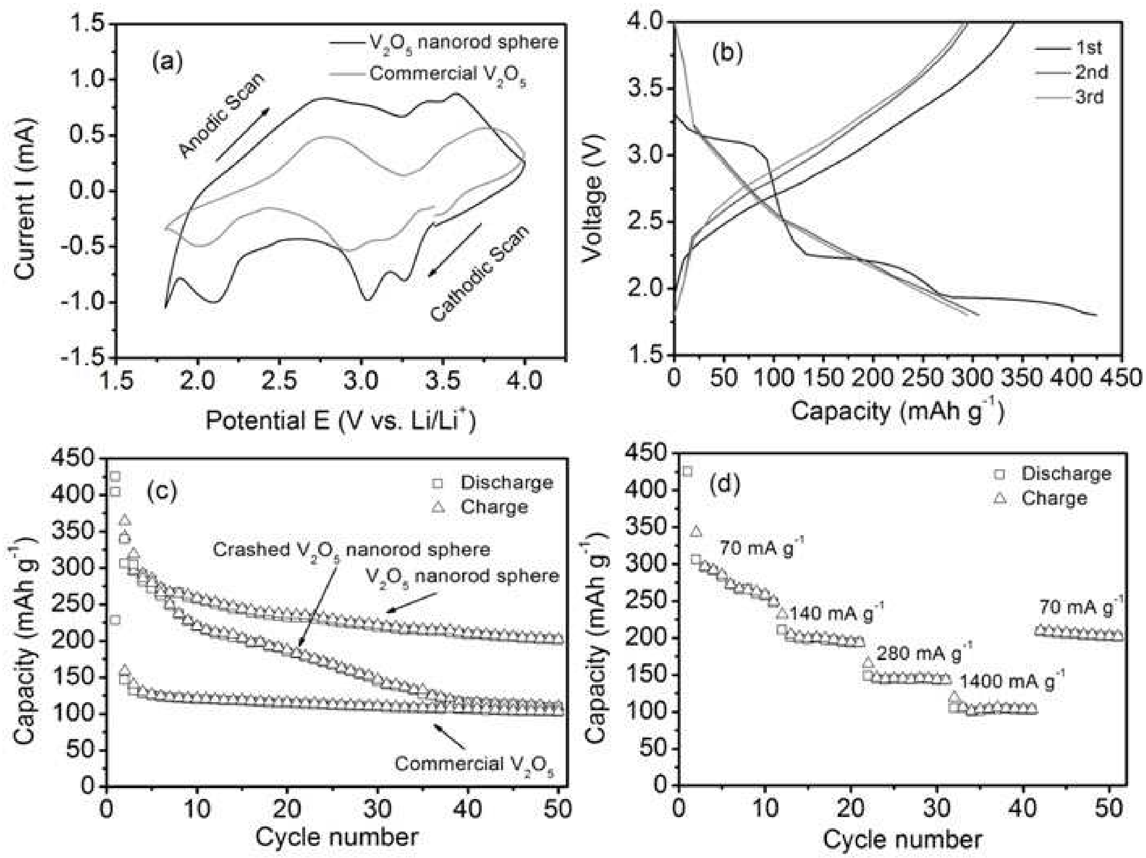

Figure 5. (a) The CV curves of electrodes made from V_2O_5 nanorod spheres and commercial V_2O_5 particles cycled in a voltage range of 1.8 to 4.0 V (*vs.* Li/Li^+) at a scan rate of 1 mV s^{-1}. The peak currents were normalized to their active mass. (b) The charge/discharge curves of V_2O_5 nanorod spheres for the first three cycles between 1.8 and 4.0 V at a current density of 70 mA g^{-1}. (c) Comparison of the cycling stability of electrodes made from the nanorod spheres, crashed nanorod spheres, and commercial V_2O_5 particles cycled between 1.8 and 4.0 V at a current density of 70 mA g^{-1}.

(d) Rate-capability of electrode made from V_2O_5 nanorod spheres cycled between 1.8 and 4.0 V at different current densities of 70, 140, 280, 1400 mA g^{-1}, respectively.

Galvanostatic charge/discharge experiments were further conducted to quantify the storage capacity of both electrodes. Figure 5b shows the charge/discharge curves of the nanorod-spheres-based electrode for the first three cycles in a voltage window of 1.8–4.0 V at a current density of 70 mA g^{-1}. On the first discharge, the electrode exhibited a typical voltage profile of lithium insertion into orthorhombic V_2O_5. After the cell was discharged to 1.8 V, a total capacity of 425 mAh g^{-1} can be achieved, which is close to the theoretical capacity of V_2O_5 with intercalation of 2.5 lithium-ion (370 mAh g^{-1}), if considering some irreversible capacity contribution from proton replacement by lithium-ion or other surface reactions at the first cycle [37]. Three voltage plateaus due to the phase transitions (from α-V_2O_5 to ε-$Li_{0.5}V_2O_5$, δ-LiV_2O_5, γ-$Li_2V_2O_5$ and ω-$Li_3V_2O_5$) associated with lithium-ion intercalation were observed on the first discharge curve. The multi-step voltage plateaus disappeared in the following cycles, which was in agreement with the CV test (Figure S2) and was consistent with previous reports [35,38]. In contrast, the commercial V_2O_5-based electrode showed similar phase transition behavior but with a much lower irreversible capacity of 228 mAh g^{-1}.

Note that for various V_2O_5-based lithium electrodes, a common issue is their rapid capacity decay due to structure and volume changes during cycling [18, 19]. Thus, improving the cycling stability of V_2O_5 electrode has been the main topic. Nevertheless, our unique nanorod-assembled sphere architecture does endow the V_2O_5 electrodes with excellent cycling stability. Figure 5c shows cycling performance of the nanorod-sphere- and commercial V_2O_5-based electrodes cycled between 1.8 and 4.0 V at a current density of 70 mA g^{-1}. The nanorod spheres were able to deliver a discharge capacity of 306 mAh g^{-1} at the 2^{nd} cycle or a capacity of 232 mAh g^{-1} and 201 mAh g^{-1} at the 20^{th} and 50^{th} cycles, respectively. The average capacity fading rate was about 0.68 % per cycle, indicating a good cycling stability. By comparison, the commercial V_2O_5 exhibited a much lower capacity of only 146 mAh g^{-1} at the 2^{nd} cycle and 102 mAh g^{-1} at the 50^{th} cycle. Note that some other nanostructured V_2O_5 electrodes may show similar capacity at initial cycles, but with much faster capacity fading [39,40].

To further confirm that the nanorod-sphere structure is responsible for the outstanding cycling stability, we crashed the nanorod structure (see SEM image in Figure S3) and tested their lithium storage performance under the same condition. As shown in Figure 5c, the electrode made from the crashed sample still exhibited a high discharge capacity of 404 mAh g^{-1} at the initial cycle, but showed a rapid capacity fading to a rather low value of 109 mAh g^{-1} after 50 cycles. This study clearly demonstrates that the nanorod-sphere structure does significantly enhance the cycling stability.

Besides the improved capacity and stability, the nanorod-sphere electrodes also showed better rate-capability. Figure 5d shows the capacities of the nanorod-sphere electrodes at different charge/discharge current densities. These electrodes can deliver a reversible capacity of 306 mAh g^{-1} at 70 mA g^{-1}, 211 mAh g^{-1} at 140 mA g^{-1} and 105 mAh g^{-1} at 1400 mA g^{-1}. Moreover, after 40 cycles, a capacity of 225 mAh g^{-1} was achieved when the charge/discharge current density was returned to 70 mA g^{-1}, further confirming the good cycling stability. However, the commercial V_2O_5 can only deliver a capacity of 19 mAh g^{-1} at current of 1400 mA g^{-1} (Figure S4) due to slower lithium diffusion in the bulk electrodes. Such impressive rate performance is attributed to the low-dimension structure of the nanorods that enables fast lithium diffusion, as well as the porous channels that supports efficient electrolyte transport. Note that such rate capability is better than that of submicron spherical V_2O_5 reported in the literature [41,42]. Although electrospun-V_2O_5 electrode showed similar capacity bur their rate capabilities were not reported [43].

2.2 LiV_3O_8 nanorod spheres

Besides V_2O_5 nanorod spheres, nanorod-spheres of LiV_3O_8 were also synthesized using a similar process. Figure 6a shows XRD of the LiV_3O_8 nanorod spheres sintered at 400 °C, suggesting a layered-type LiV_3O_8 (JCPDS 72-1193) structure of which the diffraction peaks can be assigned to a monoclinic phase with a space group of $P2_1/m$. Figure 6b displays the SEM image of the LiV_3O_8 nanorod spheres, showing morphology similar to that of the V_2O_5 particles. The sizes of the spheres are ranged from 100 to 500 nm in diameter. Similarly, these spheres consist of nanorods with diameters of 10-30 nm and length of about 100 nm (inset of Figure 6b). Table S1 summarizes the surface area and the pore structure properties of LiV_3O_8 nanorod spheres, revealing porous structure similar to that of the V_2O_5 nanorod spheres.

Similar to V_2O_5, previous LiV_3O_8-based electrodes also normally showed rapid capacity decay due to structure and volume changes during cycling [44,45]. Nevertheless, our unique nanorod sphere architecture could also endow the LiV_3O_8 electrodes with excellent cycling stability. Figure 6c shows the cycling performance of the LiV_3O_8 nanorod-sphere electrode cycled between 2.0 and 4.0 V at a current density of 100 mA g^{-1}. The nanorod-sphere electrodes presented an initial discharge capacity of 324 mAh g^{-1}. Hereafter, the discharge capacity decreased to 284 mAh g^{-1} and 262 mAh g^{-1} at the 20th and 50th cycles, respectively. The average capacity fading rate was about 0.38 % per cycle, which was lower than other nanostructured LiV_3O_8 electrodes with similar initial capacity at initial cycle [46,47].

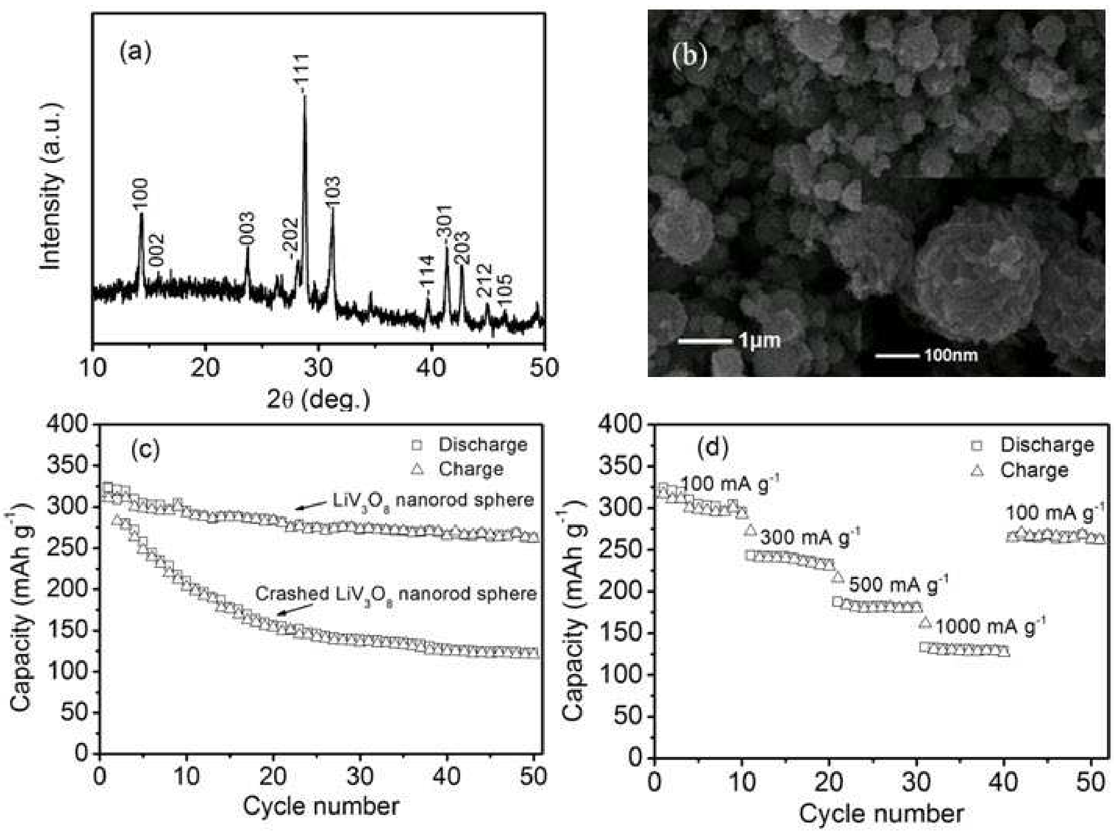

Figure 6. (a) XRD patterns of the LiV_3O_8 nanorod spheres. (b) SEM image of the LiV_3O_8 nanorod spheres. (c) Comparison of the capacity retention of electrodes made from the LiV_3O_8 nanorod spheres and the crashed LiV_3O_8 nanorod spheres cycled between 2.0 and 4.0 V at a current density of 100 mA g^{-1}. (d) Rate-capability of electrode made from LiV_3O_8 nanorod spheres cycled between 2.0 and 4.0 V at different current densities of 100, 300, 500 and 1000 mA g^{-1}, respectively.

Similarly, we also crashed the LiV_3O_8 nanorod-sphere structure (see SEM image in Figure S5) and examined their lithium storage performance. As shown in Figure 6c, the electrodes made from the crashed sample still delivered a high discharge capacity of 323 mAh g^{-1} at initial cycle, but it faded quickly to a rather low value of 122 mAh g^{-1} at the 50^{th} cycle. Therefore, the significantly enhanced cycling stability should be ascribed to the hierarchical nanorod-sphere structure.

In addition, the rate-capability was consistently improved. Figure 6d shows the capacities of the nanorod-sphere electrodes at various current densities. When operated at current density of 100 mA g^{-1}, 300 mA g^{-1}, 500 mA g^{-1}, and 1000 mA g^{-1}, these electrodes were able to deliver a reversible capacity of 324 mAh g^{-1}, 243 mAh g^{-1}, 187 mAh g^{-1}, and 133 mAh g^{-1}, respectively. Moreover, a capacity of 265 mAh g^{-1} was achieved after 40 cycles at 100 mA g^{-1}, further confirming the good cycling stability. Such impressive rate performance is also attributed to the low-dimension structure of the nanorods and the porous channels. It should be mentioned that such rate capability is also better than that of micron-rod LiV_3O_8 reported in the literature [48].

2.3 Fe_3O_4 nanocrystal spheres

To further examine the superiority of hierarchical structure, iron oxide was used as a model material for anode application. Different from making V_2O_5 structures using molecular precursor solutions, Fe_3O_4 nanocrystal spheres was made by directly assembling Fe_3O_4 nanocrystals. The prepared Fe_3O_4 nanocrystal spheres were first examined by XRD. Figure S6 shows that the pattern of the annealed particles can be indexed as face-centered cubic Fe_3O_4 (JCPDS 65-3107, a = b = c = 8.390 Å). The size and morphology of the Fe_3O_4 particles were examined by SEM. Figure 7a shows that most of the Fe_3O_4 particles present spherical-shape with diameter of around 100-600 nm. It can be clearly seen that these spheres are composed of many nanocrystals with average size of about 8 nm; these nanocrystals are interconnected together forming a porous structure (inset of Figure 7a). Compared with the Fe_3O_4 nanocrystals, the Fe_3O_4 nanocrystal spheres exhibit lower surface area and smaller pore volume (Table S1). However, the Fe_3O_4 nanocrystal spheres possess larger average pore size than the Fe_3O_4 nanocrystals, which is expected to facilitate electrolyte penetration into the electrode particles, and provide favorable transport kinetics for lithium ions.

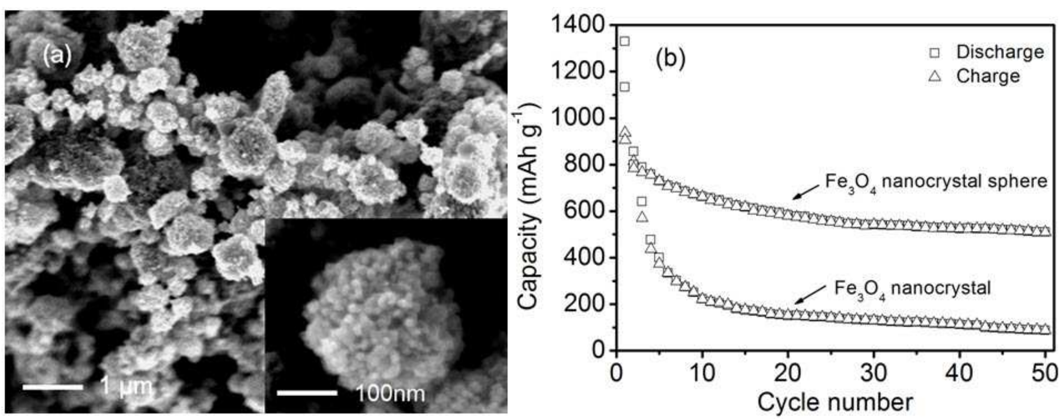

Figure 7. (a) SEM image of Fe_3O_4 nanocrystal spheres. (b) Comparison of the capacity retention of electrodes made from the Fe_3O_4 nanocrystal spheres and the Fe_3O_4 nanocrystals cycled between 0.005 and 3.0 V at a current density of 100 mA g^{-1}.

In order to examine the cycling stability of Fe_3O_4 nanocrystal spheres as lithium anode material, the capacity retention of Fe_3O_4 nanocrystal spheres and Fe_3O_4 nanocrystals is compared in Figure 7b. Compared with that of Fe_3O_4 nanocrystals, the specific capacity of

Fe_3O_4 nanocrystal spheres anode is greatly enhanced at a current density of 100 mA g^{-1}. The irreversible capacity loss in the first cycle can be attributed to the formation of a SEI layer. At the 2^{nd} cycle, the Fe_3O_4 nanocrystal-sphere electrode exhibited a discharge capacity of 857 mAh g^{-1} at a current density of 100 mA g^{-1}. The reversible capacity of Fe_3O_4 nanocrystal spheres remained to be approximately 511 mAh g^{-1} at the end of 50^{th} cycle, while it was better than those of the porous Fe_3O_4 spheres [49] and hollow Fe_3O_4 spheres synthesized via hydrothermal method [50]. This can be attributed to the structural robustness of the nanocrystal-sphere structure. Although the Fe_3O_4 nanocrystals electrode had a discharge capacity of 800 mAh g^{-1} at the 2^{nd} cycle, it faded quickly during the subsequent cycles: the electrode lost more than 80% of the initial capacity after 50 cycles.

The above results clearly demonstrate that nanorod/nanocrystal spheres have higher lithium ion storage capacity, better cycling stability, and better rate capability than native low-dimension nanorods or nanocrystals. The remarkable improvement of the electrochemical performance could be attributed to the following reasons: (a) the networks of interconnected nanoparticles could significantly facilitate the electrolyte to pass through the whole sphere structure, and therefore more surface sites are accessible when lithium ions react with the active materials; (b) hierarchical spheres have robust structures, which may greatly decrease the possible structural destruction induced by large lithium ion insertion, especially at high charge/discharge rates; (c) the porous structure keeps the electrode-electrolyte contact and shortens the lithium ions diffusion distance, which may improves the lithium ion transport [51-54]. In addition, we note that the electrochemical performance of such spheres could be further improved by introducing carbon matrices to facilitate electronic conductivity and electron transport, which will be reported separately.

3. Conclusions

In summary, using an efficient aerosol-spraying process, we successfully demonstrated a class of high-performance lithium-storage architectures by constructing oxide-based hierarchical spheres. Such spheres are constructed from interconnected nanorod or nanocrystal networks with hierarchically porous structure, which simultaneously provides structure stability and fast lithium insertion/extraction kinetics. These properties endow the electrodes with high capacity, excellent cycling stability and good rate capability. Considering the generality of our method, we believe this materials strategy can be extended to synthesize many other metal oxides and composites for energy storage and other applications.

Acknowledgements

CL and ZC contributed equally to this work. This research work was supported as part of the Molecularly Engineered Energy Materials, an Energy Frontier Research Center funded by the U.S. Department of Energy, Office of Science, Office of Basic Energy Sciences under award DE-SC001342, and also supported by National Natural Science Foundation of China (No. 51272028). The authors also thank for the support from General Motor Inc. and IMRA Inc. America.

References

[1] Tarascon, J. M.; Armand, M. Issues and challenges facing rechargeable lithium batteries. *Nature* **2001**, *414*, 359-367.

[2] Arico, A. S.; Bruce, P.; Scrosati, B.; Tarascon, J. M.; Schalkwijk, W. V. Nanostructured materials for advanced energy conversion and storage devices. *Nat. Mater.* **2005**, *4*, 366-377.

[3] Sakamoto, J. S.; Dunn, B. Hierarchical battery electrodes based on inverted opal structures. *J. Mater. Chem.* **2002**, *12*, 2859-2861.

[4] Guo, Y. G.; Hu, J. S.; Wan, L. J. Nanostructured materials for electrochemical energy conversion and storage devices. *Adv. Mater.* **2008**, *20*, 2878-2887.

[5] Liu, D. W.; Cao, G. Z. Engineering nanostructured electrodes and fabrication of film electrodes for efficient lithium ion intercalation. *Energy Environ. Sci.* **2010**, *3*, 1218-1237.

[6] Cao, A.-M., Hu, J.-S.; Liang, H.-P.; Wan, L.-J., Self-Assembled Vanadium Pentoxide (V_2O_5) Hollow Microspheres from Nanorods and Their Application in Lithium-Ion Batteries. *Angewandte Chemie International Edition* **2005**, 44 (28), 4391-4395.

[7] Chen, J. S.; Tan, Y. L.; Li, C. M.; Cheah, Y. L.; Luan, D.; Madhavi, S.; Boey, F. Y. C.; Archer, L. A.; Lou, X. W., Constructing Hierarchical Spheres from Large Ultrathin Anatase TiO_2 Nanosheets with Nearly 100% Exposed (001) Facets for Fast Reversible Lithium Storage. *Journal of the American Chemical Society* **2010**, 132(17), 6124-6130.

[8] Zhang, W. M.; Hu, J. S.; Guo, Y. G.; Zheng, S. F.; Zhong, L. S.; Song, W. G.; Wan, L. J., Tin-Nanoparticles Encapsulated in Elastic Hollow Carbon Spheres for High-Performance Anode Material in Lithium-Ion Batteries. *Advanced Materials* **2008**, 20 (6), 1160-1165.

[9] Magasinski, A.; Dixon, P.; Hertzberg, B.; Kvit, A.; Ayala, J.; Yushin, G., High-performance lithium-ion anodes using a hierarchical bottom-up approach. *Nat Mater* **2010**, 9 (4), 353-358.

[10] Jung, H.-G.; Myung, S.-T.; Yoon, C. S.; Son, S.-B.; Oh, K. H.; Amine, K.; Scrosati, B.; Sun, Y.-K., Microscale spherical carbon-coated $Li_4Ti_5O_{12}$ as ultra high power anode material for lithium batteries. *Energy & Environmental Science* **2011**, 4, 1345-1351.

[11] Lim, S.; Yoon, C. S.; Cho, J., Synthesis of Nanowire and Hollow $LiFePO_4$ Cathodes for High-Performance Lithium Batteries. *Chemistry of Materials* **2008**, 20(14), 4560-4564.

[12] Nordlinder, S.; Nyholm, L.; Gustafsson, T.; Edström, K. Lithium insertion into vanadium oxide nanotubes: electrochemical and structural aspects. *Chem. Mater.* **2006**, *18*, 495-503.

[13] Chan, C. K.; Peng, H. L.; Twesten, R. D.; Jarausch, K.; Zhang, X. F.; Cui, Y. Fast,

completely reversible Li insertion in vanadium pentoxide nanoribbons. *Nano. Lett.* **2007**, *7*, 490-495.

[14] Xu, H. Y.; Wang, H.; Song, Z. Q.; Wang, Y. W.; Yan, H.; Yoshimura, M. Novel chemical method for synthesis of LiV_3O_8 nanorods as cathode materials for lithium ion batteries. *Electrochim. Acta* **2004**, *49*, 349-353.

[15] Pan, A. Q.; Liu, J.; Zhang, J. G.; Cao, G. Z.; Xu, W.; Nie, Z. M.; Jie, X.; Choi, D. W.; Arey, B. W.; Wang, C. M.; Liang, S. Q. Template free synthesis of LiV_3O_8 nanorods as a cathode material for high-rate secondary lithium batteries. *J. Mater. Chem.* **2011**, *21*, 1153-1161.

[16] Taberna, P. L.; Mitra, S.; Poizot, P.; Simon, P.; Tarascon, J. M. High rate capabilities Fe_3O_4-based Cu nano-architectured electrodes for lithium-ion battery applications. *Nat. Mater.* **2006**, *5*, 567-573.

[17] Cui, Z. M.; Jiang, L. Y.; Song, W. G.; Guo, Y. G. High-yield gas−liquid interfacial synthesis of highly dispersed Fe_3O_4 nanocrystals and their application in lithium-ion batteries. *Chem. Mater.* **2009**, *21*, 1162-1166.

[18] Lantelme, F.; Mantoux, A.; Groult, H.; Lincot, D. Electrochemical study of phase transition processes in lithium insertion in V_2O_5 electrodes. *J. Electrochem. Soc.* **2003**, *150*, A1202-A1208.

[19] Desilvestro, J.; Haas, O. Metal oxide cathode materials for electrochemical energy storage: a review. *J. Electrochem. Soc.* **1990**, *137*, 5C-22C.

[20] Ji, L. W.; Tan, Z. K.; Kuykendall, T. R.; Aloni, S.; Xun, S. D.; Lin, E.; Battaglia, V.; Zhang, Y. G. Fe_3O_4 nanoparticle-integrated graphene sheets for high-performance half and full lithium ion cells. *Phys. Chem. Chem. Phys.* **2011**, *13*, 7170-7177.

[21] Mohan, V. M.; Hu, B.; Qiu, W. L.; Chen, W. Synthesis, structural, and electrochemical performance of V_2O_5 nanotubes as cathode material for lithium battery. *J. Appl. Electrochem.* **2009**, *39*, 2001-2006.

[22] Feng, C. Q.; Chew, S. Y.; Guo, Z. P.; Wang, J. Z.; Liu, H. K. An investigation of polypyrrole-LiV_3O_8 composite cathode materials for lithium-ion batteries. *J. Power Sources* **2007**, *174*, 1095-1099.

[23] Liu, H.; Wang, G. X.; Wang, J. Z.; Wexler, D. Magnetite/carbon core-shell nanorods as

anode materials for lithium-ion batteries. *Electrochem. Comm.* **2008**, *10*, 1879-1882.

[24] Li, G. C.; Pang, S. P.; Jiang, L.; Guo, Z. Y.; Zhang, Z. K. Environmentally friendly chemical route to vanadium oxide single-crystalline nanobelts as a cathode material for lithium-ion batteries. *J. Phys. Chem. B* **2006**, *110*, 9383-9386.

[25] Idris, N. H.; Rahman, M. M.; Wang, J. Z.; Chen, Z. X.; Liu, H. K. Synthesis and electrochemical performance of LiV_3O_8/carbon nanosheet composite as cathode material for lithium-ion batteries. *Compos. Sci. Technol.* **2011**, *71*, 343-349.

[26] Muraliganth, T.; Murugan, A. V.; Manthiram, A.; Facile synthesis of carbon-decorated single-crystalline Fe_3O_4 nanowires and their application as high performance anode in lithium ion batteries. *Chem. Comm.* **2009**, 7360-7362.

[27] Ng, S. H.; Chew, S. Y.; Wang, J.; Wexler, D.; Tournayre, Y.; Konstantinov, K.; Liu, H. K. Synthesis and electrochemical properties of V_2O_5 nanostructures prepared via a precipitation process for lithium-ion battery cathodes. *J. Power Sources* **2007**, *174*, 1032-1035.

[28] Yang, H.; Li, J.; Zhang, X. G.; Jin, Y. L. Synthesis of LiV_3O_8 nanocrystallites as cathode materials for lithium ion batteries. *J. Mater. Process. Technol.* **2008**, 207, 265-270.

[29] Yoon, T.; Chae, C.; Sun, Y. K.; Zhao, X.; Kung, H. H.; Lee, J. K. Bottom-up in situ formation of Fe_3O_4 nanocrystals in a porous carbon foam for lithium-ion battery anodes. *J. Mater. Chem.* **2011**, *21*, 17325-17330.

[30] Xu, Y.; Liu, Q.; Zhu, Y.; Liu, Y.; Langrock, A.; Zachariah, M. R.; Wang, C., Uniform Nano-Sn/C Composite Anodes for Lithium Ion Batteries. *Nano Letters* **2013**,13, 470-474.

[31] Park, S. H.; Yoon, C. S.; Kang, S. G.; Kim, H. S.; Moon, S. I.; Sun, Y. K., Synthesis and structural characterization of layered $Li[Ni_{1/3}Co_{1/3}Mn_{1/3}]O_2$ cathode materials by ultrasonic spray pyrolysis method. *Electrochimica Acta* **2004**, 49, (4), 557-563.

[32] Jung, D. S.; Hwang, T. H.; Park, S. B.; Choi, J. W., Spray Drying Method for Large-Scale and High-Performance Silicon Negative Electrodes in Li-Ion Batteries. *Nano Letters* **2013**, 13(5), 2092-2097.

[33] Chen, X. L.; Li, L.; Sun, X. M.; Liu, Y. P.; Luo, B.; Wang, C. C.; Bao. Y. P.; Xu, H.; Peng, H. S. Magnetochromatic polydiacetylene by incorporation of Fe_3O_4 nanoparticles. *Angew. Chem. Int. Ed.* **2011**, *50*, 5486-5489.

[34] Galy, J. Vanadium pentoxide and vanadium oxide bronzes-Structural chemistry of single (S) and double (D) layer $M_xV_2O_5$ phases. *J. Solid State Chem.* **1992**, *100*, 229-245.

[35] Delmas, C.; Cognac-Auradou, H.; Cocciantelli, J. M.; Ménétrier, M.; Doumerc, J. P. The $Li_xV_2O_5$ system: an overview of the structure modifications induced by the lithium intercalation. *Solid State Ionics* **1994**, *69*, 257-264.

[36] Pan, A.; Wu, H. B; Zhang, L.; Lou, X. W. *Energy Environ. Sci.*, **2013**, *6*, 1476-1479.

[37] Borghols, W. J. H.; Lützenkirchen-Hecht, D.; Haake, U.; Chan, W.; Lafont, U.; Kelder, E. M.; Eck van, E. R. H.; Kentgens, A. P. M.; Mulder, F. M.; Wagemaker, M. Lithium storage in amorphous TiO_2 nanoparticles. *J. Electrochem. Soc.* **2010**, *157*, A582-A588.

[38] Pan, A.; Wu, H. B; Yu, L.; Lou, X. W. *Angew. Chem. Int. Ed.* **2013**, *52*, 2226-2230.

[39] Zhu, D.; Liu, H.; Lv, L.; Yao, Y. D.; Yang, W. Z. Hollow microspheres of V_2O_5 and Cu-doped V_2O_5 as cathode materials for lithium-ion batteries. *Scr. Mater.* **2008**, 59, 642-645.

[40] Rui, X. H.; Zhu, J. X.; Sim, D. H.; Xu, C.; Zeng, Y.; Hng, H. H.; Lim, T. M.; Yan, Q. Y. Reduced graphene oxide supported highly porous V_2O_5 spheres as a high-power cathode material for lithium ion batteries. *Nanoscale* **2011**, *3*, 4752-4758.

[41] Ng, S. H.; Patey, T. J.; Büchel, R.; Krumeich, F.; Wang, J. Z.; Liu, H. K.; Pratsinis, S. E.; Novak, P. Flame spray-pyrolyzed vanadium oxide nanoparticles for lithium battery cathodes. *Phys. Chem. Chem. Phys.* **2009**, *11*, 3748-3755.

[42] Chen, Y.; Liu, H.; Ye, W. Preparation and electrochemical properties of submicron spherical V_2O_5 as cathode material for lithium ion batteries. *Scr. Mater.* **2008**, *59*, 372-375.

[43] Mai, L. Q.; Xu, L.; Han, C. H.; Xu, X.; Luo, Y. Z.; Zhao, S. Y.; Zhao, Y. L. Electrospun ultralong hierarchical vanadium oxide nanowires with high performance for lithium ion batteries. *Nano. Lett.* **2010**, *10*, 4750-4755.

[44] Jouanneau, S.; Salle, A. L. G. L.; Verbaere, A.; Deschamps, M.; Lascaud, S.; Guyomard, D. Influence of the morphology on the Li insertion properties of $Li_{1.1}V_3O_8$. *J. Mater. Chem.* **2003**, *13*, 921-927.

[45] Jouanneau, S.; Salle, A. L. G. L.; Verbaere, A.; Guyomard, D. The origin of capacity fading upon lithium cycling in $Li_{1.1}V_3O_8$. *J. Electrochem. Soc.* **2005**, *152*, A1660-A1667.

[46] Brylev, O. A.; Shlyakhtin, O. A.; Egorov, A. V.; Tretyakov, Y. D. Phase formation and electrochemical properties of cryochemically processed $Li_{1+x}V_3O_8$ materials *J. Power Sources* **2007**, *164*, 868-873.

[47] Ju, S. H.; Kang, Y. C. Morphological and electrochemical properties of LiV_3O_8 cathode powders prepared by spray pyrolysis. *Electrochim. Acta* **2010**, *55*, 6088-6092.

[48] Sakunthala, A.; Reddy, M. V.; Selvasekarapandian, S.; Chowdari, B. V. R.; Selvin, P. C. Preparation, characterization, and electrochemical performance of lithium trivanadate rods by a surfactant-assisted polymer precursor method for lithium batteries. *J. Phys. Chem. C* **2010**, *114*, 8099-8107.

[49] Wang, G.; Liu, T.; Xie, X. L.; Ren, Z. Y.; Bai, J. B.; Wang, H. Structure and electrochemical performance of Fe_3O_4/graphene nanocomposite as anode material for lithium-ion batteries. *Mater. Chem. Phys.* **2011**, *128*, 336-340.

[50] Zhang, W. D.; Wang, X. Y.; Zhou, H. H.; Chen, J. T.; Zhang, X. X. Fe_3O_4-C open hollow sphere assembled by nanocrystals and its application in lithium ion battery. *J. Alloy. Compd.* **2012**, *521*, 39-44.

[51] Wu, Y. M.; Wen, Z. H.; Li, J. H. Hierarchical carbon-coated $LiFePO_4$ nanoplate microspheres with high electrochemical performance for Li-ion batteries. *Adv. Mater.* **2011**, *23*, 1126-1129.

[52] Magasinski, A.; Dixon, P.; Hertzberg, B.; Kvit, A.; Ayala, J.; Yushin, G. High-performance lithium-ion anodes using a hierarchical bottom-up approach. *Nat. Mater.* **2010**, *9*, 353-358.

[53] Ren, Y.; Hardwick, L. J.; Bruce, P. G. Lithium intercalation into mesoporous anatase with an ordered 3D pore structure. *Angew. Chem. Int. Ed.* **2010**, *49*, 2570-2574.

[54] Wang, Y. G.; Li, H. Q.; He, P.; Hosono, E.; Zhou, H. S. Nano active materials for lithium-ion batteries. *Nanoscale* **2010**, *2*, 1294-1305.

The table of contents

Better lithium-storage architectures based on hierarchically assembled nanorods or nanocrystals were developed using an efficient aerosol-spraying process.

ToC Figure: